

## EMPIRICAL CONSTRAINTS ON THE OBLATENESS OF AN EXOPLANET

JOSHUA A. CARTER & JOSHUA N. WINN

Department of Physics, and Kavli Institute for Astrophysics and Space Research,  
Massachusetts Institute of Technology, Cambridge, MA 02139  
carterja@mit.edu, jwinn@mit.edu

*Accepted for publication in The Astrophysical Journal*

### ABSTRACT

We show that the gas giant exoplanet HD 189733b is less oblate than Saturn, based on *Spitzer Space Telescope* photometry of seven transits. The observable manifestations of oblateness would have been slight anomalies during the ingress and egress phases, as well as variations in the transit depth due to spin precession. Our nondetection of these effects gives the first empirical constraints on the shape of an exoplanet. The results are consistent with the theoretical expectation that the planetary rotation period and orbital period are synchronized, in which case the oblateness would be an order of magnitude smaller than our upper limits. Conversely, if HD 189733b is assumed to be in a synchronous, zero-obliquity state, then the data give an upper bound on the quadrupole moment of the planet ( $J_2 < 0.068$  with 95% confidence) that is too weak to constrain the interior structure of the planet. An Appendix describes a fast algorithm for computing the transit light curve of an oblate planet, which was necessary for our analysis.

*Subject headings:* methods: numerical—stars: planetary systems—techniques: photometric

### 1. INTRODUCTION

Planets are not exactly spherical. Departures from sphericity are caused by rotation, external gravitational tides, and material rigidity. For gas giant planets, material rigidity is not important, but tides and rotation are very important. The tidal bulges raised on “hot Jupiters” by their parent stars allow angular momentum to be exchanged between the planetary rotational and orbital motions, and result in long-term energy dissipation (Goldreich & Soter 1966, Peale 1999, Murray & Dermott 2000). As for rotation, both Jupiter and Saturn are visibly flattened due to centrifugal forces, with their polar radii shorter than equatorial radii by 6.5% and 9.8%, respectively (Lindal et al. 1981, 1985).

It would be of great interest to determine the shapes of planets outside of the Solar System. Knowledge of the equilibrium shape of an exoplanet would provide information on its rotation rate and internal density structure, which in turn would give clues about its formation and evolution. One way this knowledge might be gained is through precise photometry of exoplanetary transits. Seager & Hui (2002) and Barnes & Fortney (2003) calculated the difference between the transit light curve of an oblate planet and of a spherical planet with the same cross-sectional area. Unfortunately the oblateness-induced signal is expected to be quite small for most of the currently known transiting planets because their rotation periods are expected to be tidally synchronized with their  $\sim 3$  day orbital periods (much longer than the  $\approx 10$  hr rotation periods of Jupiter and Saturn). For the representative case of HD 209458b, Barnes & Fortney (2003) found the amplitude of the theoretically expected oblateness-induced signal to be  $0.1 \mu\text{mag}$ , well below the limiting precision of any current photometer.

The goal of this work was to place the first *empirical* constraints on the shape of an exoplanet. While the assumption of spin-orbit synchronization seems reasonable, it is worth checking on such assumptions whenever possible. It is also useful to know the upper limits that can be achieved with current data, with an eye toward planning future observations and photometric instruments. By selecting the most favorable

planet and the best available data, we find that an oblateness as large as that of Saturn can be ruled out, and an oblateness as large as that of Jupiter is also ruled out if it is accompanied by a moderate obliquity. In addition, we model the effects of spin precession on transit light curves, which were not considered by Seager & Hui (2002) or Barnes & Fortney (2003), and provide a fast algorithm for calculating the light curve of an oblate planet.

This paper is organized as follows. In § 2 we review the relevant physics and geometry. In § 3, we present seven *Spitzer* 8  $\mu\text{m}$  transit observations of the well-studied system HD 189733 (Bouchy et al. 2005). In § 4, we present the results of fitting a parameterized model to the data, including the sky-projected oblateness and obliquity in addition to the usual transit parameters. We consider the case of a fixed orientation for the planet (§ 4.1) as well as uniform precession of the spin axis (§ 4.2). In the latter case we are able to constrain the *true* oblateness and obliquity as well as the precession period. In § 5 we summarize our methods and results and suggest some possible extensions. Appendix A describes the algorithm we used to produce transit light curves of oblate planets.

### 2. REVIEW OF PLANETARY OBLATENESS

#### 2.1. Rotation

A uniformly rotating self-gravitating fluid takes on the figure of an oblate spheroid, with its minimum diameter along the axis of rotation (Eddington 1926). The shape may be quantified by the *oblateness* (or *flattening*) parameter  $f$ , defined as

$$f = \frac{R_{\text{eq}} - R_{\text{pol}}}{R_{\text{eq}}} \quad (1)$$

where  $R_{\text{eq}}$  and  $R_{\text{pol}}$  are the equatorial and polar radii, respectively (Murray & Dermott 2000). The angle between the polar axis and the orbital axis is the *obliquity*  $\theta$ .

The relationship between  $f$  and the rotation period  $P_{\text{rot}}$  is found by identifying the contours of constant potential, where the potential has both gravitational and centrifugal terms. The

gravitational terms are

$$V_g(r, \psi) = -\frac{GM_p}{r} \left[ 1 - \sum_{n=2}^{\infty} J_n \left( \frac{R_{\text{eq}}}{r} \right)^n \mathcal{P}_2(\cos \psi) \right] \quad (2)$$

where  $J_n$  are the spherical mass moments<sup>1</sup> associated with rotation,  $\psi$  is the planetary colatitude, and  $\mathcal{P}_n$  is the Legendre polynomial of degree  $n$ . The centrifugal terms are

$$V_c(r, \psi) = \frac{1}{3} \Omega^2 r^2 [\mathcal{P}_2(\cos \psi) - 1], \quad (3)$$

where  $\Omega \equiv 2\pi/P_{\text{rot}}$  is the rotational angular frequency. Assuming that the quadrupole moment  $J_2$  is the most important moment, the total potential is

$$V_{\text{tot}}(r, \psi) = -\frac{GM_p}{r} + \left( \frac{GM_p R_{\text{eq}}^2}{r^3} J_2 + \frac{1}{3} \Omega^2 r^2 \right) \mathcal{P}_2(\cos \psi) - \frac{1}{3} \Omega^2 r^2. \quad (4)$$

Because the surface of the planet lies on an equipotential,  $V_{\text{tot}}(R_{\text{eq}}, \frac{\pi}{2}) = V_{\text{tot}}(R_{\text{pol}}, 0)$ , giving

$$-\frac{GM_p}{R_{\text{eq}}} \frac{1}{2} \left( \frac{GM_p}{R_{\text{eq}}} J_2 + \Omega^2 R_{\text{eq}}^2 \right) = -\frac{GM_p}{R_{\text{eq}}} + \frac{GM_p R_{\text{eq}}^2}{R_{\text{pol}}^3} J_2. \quad (5)$$

This equality implies (to leading order in  $f$ )

$$f = \frac{3}{2} J_2 + \frac{1}{2} \frac{\Omega^2 R_{\text{eq}}^3}{GM_p}. \quad (6)$$

Derivations of this relation are also given by Murray & Dermott (2000) and Hubbard (1984). Solving for  $P_{\text{rot}} = 2\pi/\Omega$ , we find

$$P_{\text{rot}} = 2\pi \sqrt{\frac{R_{\text{eq}}^3}{GM_p (2f - 3J_2)}}. \quad (7)$$

This result reduces to Eqn. (6) of Seager & Hui (2002) if the  $J_2$  term is neglected.

For Solar system planets,  $f$  is measured from direct images and  $J_2$  is measured by monitoring elliptical orbits of satellites whose orbits precess in response to the aspherical gravitational field. Table 1 gives  $f$  and  $J_2$  for planets in our Solar System, to help place our results for the exoplanet HD 189733b in context. The maximum possible value for  $f$  occurs at the rotational breakup limit, when the outward centrifugal acceleration equals the gravitational acceleration at the equator. With reference to Eqns. (2-3), this criterion gives  $f < \frac{1}{2} + \frac{3}{4} J_2$ .

Another relation between  $J_2$  and  $f$  can be obtained by assuming the planet's interior to be in a state of hydrostatic equilibrium, leading to the Darwin-Radau approximation,

$$\frac{J_2}{f} \approx -\frac{3}{10} + \frac{5}{2} \mathbb{C} - \frac{15}{8} \mathbb{C}^2. \quad (8)$$

Here,  $\mathbb{C}$  is the dimensionless moment of inertia, defined such that  $\mathbb{C} M_p R_{\text{eq}}^2$  is the moment of inertia about the spin axis (Murray & Dermott 2000). The moment of inertia of Solar

<sup>1</sup>  $J_n = \frac{1}{M_p R_{\text{eq}}^n} \int_0^{R_{\text{eq}}} \int_{-1}^{+1} r^n \mathcal{P}_n(\mu) \rho(r, \mu) 2\pi r^2 d\mu dr$

TABLE 1  
SHAPE PARAMETERS OF SOLAR  
SYSTEM PLANETS

Planet	Oblateness $f$	$J_2$
Mercury	0.00012	0.000060
Venus	0.00009	0.000004
Earth	0.00350	0.001083
Mars	0.00520	0.001960
Jupiter	0.06487	0.014736
Saturn	0.09796	0.016298
Uranus	0.02293	0.003343
Neptune	0.01708	0.003411

REFERENCES. — Murray & Dermott (2000), Barnes & Fortney (2003), Hubbard (1984).

system planets is not directly measurable but models of gas giant interiors suggest  $\mathbb{C} \approx 0.23$  (Hubbard & Marley 1989).

## 2.2. Sky projection

A transit by an oblate planet will produce a slightly different light curve than a transit by a spherical planet of the same cross-sectional area. The differences are most pronounced during the ingress and egress phases of the transit. There are also slight differences during the complete phase of the transit, due to the limb darkening of the stellar photosphere. For illustrations of these effects we refer the reader to Seager & Hui (2002) and Barnes & Fortney (2003).

The shape of a single transit light curve will depend only on the *sky projection* of the planet's figure at the time of the transit. The sky projection of an oblate or prolate spheroid (or any triaxial ellipsoid) is an ellipse. We define the *projected oblateness*  $f_{\perp}$  as  $(a-b)/a$ , where  $a$  and  $b$  are the lengths of the major and minor axes of the ellipse. We also define the *projected obliquity*  $\theta_{\perp}$  as the angle between the major axis and the transit chord. The relations between these projected quantities and the unprojected quantities  $f$  and  $\theta$  can be found with elementary geometry:

$$f_{\perp} = 1 - \sqrt{\sin^2 \theta' + (1-f)^2 \cos^2 \theta'}, \quad (9)$$

$$\tan \theta_{\perp} = \tan \theta \sin \phi, \quad (10)$$

where  $\theta'$  is the angle between the planetary rotation axis and the sky plane, given by

$$\cos^2 \theta' = \sin^2 \theta \sin^2 \phi + \cos^2 \theta, \quad (11)$$

and  $\phi$  is the azimuthal angle of the line of nodes between the planetary equator and the orbital plane, with  $\phi = 0$  corresponding to the case when the rotation axis is tipped toward the observer. A derivation of Eqn. (9) is also given by Barnes (2009).

The calculation of the transit light curve of an oblate planet is computationally intensive, because the intersection points between a circle and an ellipse are nonanalytic, and because the precision of the calculation must be very high in order to isolate the small oblateness-specific effects. In Appendix A we describe a fast algorithm that we developed for our study, building on the previous work by Seager & Hui (2002) and Barnes & Fortney (2003).

## 2.3. Spin precession

External gravitational forces will cause a planet's spin axis to precess. In particular, the spin axis of a rotationally-induced, oblate spheroidal planet will precess in response to

the gravitational torque of its host star, with a period

$$P_{\text{prec}} = \frac{2}{3} \frac{P_{\text{orb}}^2}{P_{\text{rot}}} \frac{C}{J_2} \frac{1}{\cos \theta} \quad (12)$$

where  $\theta$  is the planetary obliquity (Ward 1975). This expression assumes that the orbit is fixed, and in particular that the orbital angular momentum is much larger than the rotational angular momentum, a good approximation even for close-in giant planets rotating as fast as Jupiter or Saturn.<sup>2</sup>

For Solar system planets, the precession periods are much longer than 1 yr. For example, Saturn completes one precession cycle in  $\approx 7 \times 10^6$  yr (ignoring the effect of moons and rings; Ward & Hamilton 2004). However, because  $P_{\text{prec}}$  scales as  $P_{\text{orb}}^2$ , sufficiently close-in planets would precess with periods short enough to be directly observable. If Saturn's orbital period were changed to  $P_{\text{orb}} = 3$  days it would precess with  $P_{\text{prec}} \sim 0.6$  yr. In § 4.2, we consider how spin precession would be manifested in a collection of transit light curves.

#### 2.4. Tidal deformation

Hot Jupiters are stretched radially (along the radius vector of the orbit) due to the gravitational tide from the nearby host star. Tidal dissipation causes important long-term changes in the orbital parameters, including spin-orbit synchronization and orbital circularization. The characteristic timescale for synchronization is

$$\tau \approx \frac{4}{9} Q C \left( \frac{R_{\text{eq}}^3}{GM_p} \right) \omega_0 \left( \frac{M_p}{M_*} \right)^2 \left( \frac{a}{R_{\text{eq}}} \right)^6 \quad (13)$$

where  $\omega_0$  is the initial angular rotation frequency,  $M_p$  is the planet's mass,  $M_*$  is the stellar mass, and  $Q$  is the specific dissipation factor of the tidal oscillator (Goldreich & Soter 1966, Hubbard 1984, Guillot et al. 1996, Murray & Dermott 2000). Many investigators adopt  $Q \sim 10^{5-6}$  for gas giant planets, although there is little empirical information about  $Q$  and some indications that  $Q$  may be larger (see, e.g., Hellier et al. 2009).

The obliquity is also expected to be driven to zero as a result of tidal evolution, although in an interesting and nonuniform manner (Peale 1999). It is possible to maintain a nonzero obliquity in a so-called Cassini state (Ward 1975, Winn & Holman 2005) but for hot Jupiters the high-obliquity states are unstable (Fabrycky et al. 2007, Levrard et al. 2007).

It would be difficult to detect a radially-directed tidal bulge through transit photometry. For tidally synchronized planets, the amplitude of the rotational deformation is roughly 1/3 that of the tidal component (Murray & Dermott 2000, pg. 156). However, the long axis is closely aligned with the line of sight during transits, and consequently the sky projection of the tidal bulge is smaller than the bulge itself by a factor  $a/R_*$ . This causes a reduction in the transit signal of the radial bulge by an order of magnitude or more, compared to the rotational bulge. Therefore in this paper we consider only the deformation associated with rotation. Ragozzine & Wolf (2009) describe some potentially observable consequences of the radial bulge.

<sup>2</sup> In reality the orbital and spin axes both precess about the total angular momentum vector. The nodal precession of the orbit would be detectable in principle through changes in the transit impact parameter. However, even if HD 189733b were spinning as fast as Jupiter, the orbital angular momentum would exceed the rotational angular momentum by a factor of 1000, and the resulting inclination variation would not be detectable in the current data.

#### 2.5. Expectations for HD 189733b

In this section we use the preceding formalism and the algorithm described in the Appendix to compute theoretical light curves for the transiting exoplanet HD 189733b. This particular exoplanet was chosen because it is the most favorable case currently known for the detection of oblateness-induced signatures, owing to the bright parent star, large transit depth, midrange transit impact parameter, and the availability of a large corpus of high-precision transit data. We took the system parameters from Torres et al. (2008) and considered two different cases for the oblateness and obliquity.

First, we imagined that HD 189733b is as oblate as Saturn ( $f_{\perp} = 0.098$ ), with a projected obliquity of  $\theta_{\perp} = 45^{\circ}$ . To isolate the signal due to oblateness, we calculated the theoretical transit light curve for the oblate planet, and then subtracted the best-fitting model for a spherical planet, following Barnes & Fortney (2003). The residuals are shown in the left panel of Figure 1. An error bar is also shown, representing the forecasted precision of a 2 min sample based on the *Spitzer* data that are currently available for this planet (see § 3). This calculation suggested that the *Spitzer* data would be capable of placing physically meaningful constraints on the oblateness, and motivated our further study.

Second, we assumed that HD 189733b has been tidally synchronized with  $P_{\text{rot}} = P_{\text{orb}} = 2.2$  days. This is reasonable because for  $Q = 10^5$  and  $\omega_{\text{prim}} = 1.7 \times 10^{-4} \text{ s}^{-1}$  (Jupiter's estimated values; Guillot et al. 1996) we find  $\tau \sim 10^6$  yr, much shorter than the estimated few-Gyr main-sequence age of the star (Torres et al. 2008). Furthermore, the observation that the orbit of HD 189733b is nearly circular (Winn et al. 2007b, Knutson et al. 2007a) is independent evidence for tidal evolution, and the theoretical synchronization timescale is shorter than the circularization timescale. We estimated the rotationally-induced oblateness using the Darwin-Radau relation and Eqn. (6), finding  $f \approx 0.003$ . The right panel of Figure 1 shows the difference between a light curve of an oblate planet with  $f_{\perp} = 0.003$  and  $\theta_{\perp} = 0$ , and the best-fitting model for a spherical planet. The peak-to-peak amplitude of the residuals is approximately  $2 \times 10^{-6}$ , below the precision of the available data. Thus, if spin-orbit synchronization has been achieved, we would expect a null result from an analysis of the *Spitzer* data.

### 3. OBSERVATIONS AND DATA REDUCTION

Transits of HD 189733b have been observed with many instruments and in many bandpasses (see, e.g., Bouchy et al. 2005, Winn et al. 2007b, Pont et al. 2007, Beaulieu et al. 2008, Miller-Ricci et al. 2008, Désert et al. 2009). For our study the best available data are the 7 different transits that were observed with the *Spitzer Space Telescope* at a wavelength of  $8 \mu\text{m}$ , with the InfraRed Array Camera (IRAC; Fazio et al. 2004). They form a homogeneous and precise data set, and by virtue of the relatively long observing wavelength the data are less affected by stellar variability, star spots and limb darkening, which would otherwise confound the attempt to detect or constrain oblateness. The first of the 7 IRAC time series was presented by Knutson et al. (2007a), and the other 6 time series are based on observations by Agol et al. (2009). The elapsed time between the first and seventh transits was 1.6 yr or 268 transits. Assigning epoch zero to the second transit (on UT 30 June 2007) the observed transits have epoch numbers  $-110, 0, 1, 51, 62, 157, \text{ and } 158$ .

All 7 transits were observed with the  $8 \mu\text{m}$  channel of the

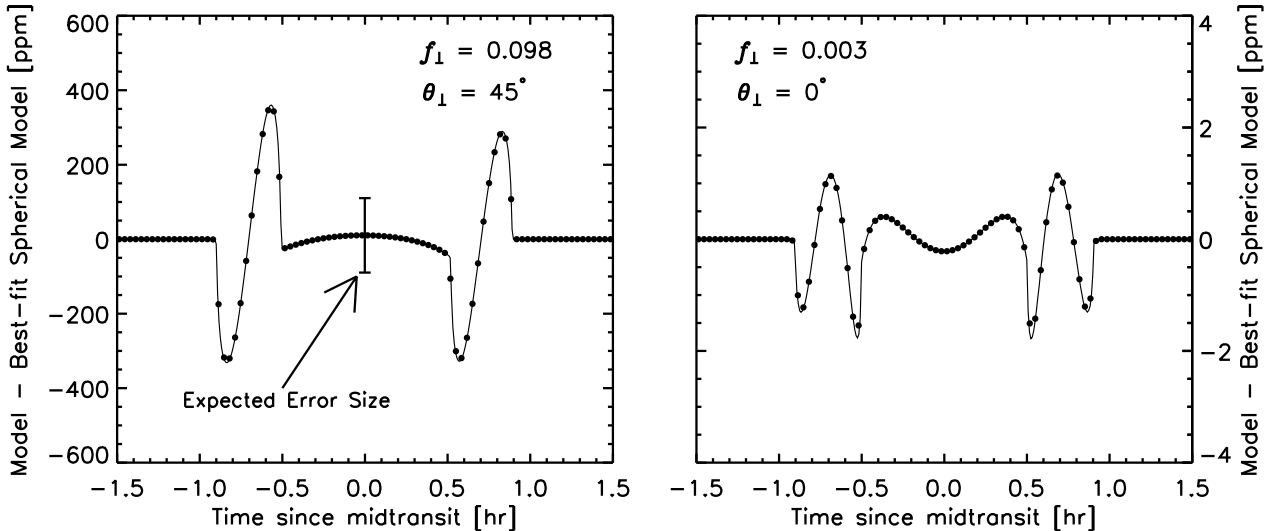


FIG. 1.— The theoretical oblateness-induced signal in the transit light curve of HD 189733b. Each panel shows the difference in the time series between the theoretical transit light curve of an oblate planet, and the best-fitting light curve of a spherical planet. In computing the theoretical light curves, all the system parameters except oblateness and obliquity were taken from Torres et al. (2008). *Left*.—Assuming HD 189733b is as oblate as Saturn and is more oblique ( $f_{\perp} = 0.098$ ,  $\theta_{\perp} = 45^{\circ}$ ). The error bar indicates the expected  $1\sigma$  noise level of a composite light curve built from seven *Spitzer* observations, binned into 2 min intervals. *Right*.—Assuming  $f_{\perp} = 0.003$  and  $\theta_{\perp} = 0$ , as appropriate for the case of a tidally synchronized planet.

IRAC instrument in subarray mode, in which only a  $32 \times 32$  pixel subarray of the detector is recorded. Images are obtained with a cadence of 0.40 s (with an integration time of 0.32 s). The data are packaged into post-calibration FITS files, each consisting of 64 images (representing a total of 26.5 s of integration time). Approximately 500 files span the transit of HD 189733b. In addition to providing excellent time resolution, the subarray mode avoids saturation even for stars as bright as HD 189733 ( $V = 7.7$ , Høg et al. 2000).

We began our data reduction with the post-calibration images, downloaded from the *Spitzer* data archive. First, we inspected each block of 64 images and determined the centroid of the target star in each image. We excluded any image in which the centroid differed by more than 0.05 pixels from the median position of all 64 images. Fewer than 1% of the images were excluded by this criterion, except for epochs 1 and 157 in which 8% and 5% of images were excluded, respectively. Next, we formed a mean image based on each block of 64 images, disregarding any pixels whose values deviated by more than  $3.5\sigma$  from the median value for that pixel. Fewer than 1% of the pixels were excluded by this criterion.

We then performed aperture photometry on the mean images, using a circular aperture of radius 4.5 pixels centered on HD 189733. To estimate the background level, we also summed the flux within several rectangular apertures located far away from both HD 189733 and its fainter companion. The background level was subtracted from the aperture sum. At this point, we had a time sequence of measurements of the relative flux density of HD 189733.

Among users of the IRAC 8  $\mu\text{m}$  channel there is a well-known systematic effect which has been called the “ramp,” because it is manifested as a gradual rise in the count rate at the beginning of an observation. It is attributed to charge trapping in the detector. It is generally modeled as a multiplicative, time-variable correction (see, e.g., Knutson et al. 2007b, Gillon et al. 2007, Nutzman et al. 2008). For each data set, we clipped the most strongly-varying portion of the ramp, and modeled the rest as a quadratic function of time (see § 4.1).

We also clipped the long post-egress portion of the time series by Knutson et al. (2007a). Figure 2 shows the final time series, after correcting for the ramp.

We assessed the noise characteristics of each time series with the `solveredwv` IDL routine<sup>3</sup>. This algorithm fits time-series data with a model in which the noise is an additive combination of white noise and  $1/f$  noise. The amplitudes of each noise component are estimated from the data as described by Carter & Winn (2009). Many of our reduction parameters (aperture size, thresholds for clipping, etc.) were chosen by attempting to minimize the time-correlated component of the noise. Our final time series had white-noise amplitudes of 586, 571, 642, 544, 560, 607 and 536 ppm, for epochs  $-110$ ,  $0$ ,  $1$ ,  $51$ ,  $62$ ,  $157$ , and  $158$ , respectively. In all cases the amplitude of the  $1/f$  component was smaller than 2 ppm. The theoretical limiting precision due to photon-counting noise was approximately 460 ppm.

## 4. ANALYSIS

### 4.1. Fixed orientation

In the analysis described in this section, we assumed the orientation of HD 189733b to be fixed in space over the 1.6 yr span of the observations. The projected oblateness parameters  $f_{\perp}$  and  $\theta_{\perp}$  were taken to be constants. In the next section we will describe an analysis in which that restriction was lifted.

The first step was a preliminary fit to all of the data, with the goal of determining the midtransit time, out-of-transit flux, and the coefficients of the ramp correction function for each epoch. These quantities are weakly correlated with the other parameters describing the light curves (including the projected oblateness and obliquity), and thus may be fixed in the subsequent analysis without significantly affecting the results.

The ramp correction function was

$$C_{\text{ramp}}(t; c_0, c_1; t_0) = 1 + c_0(t - t_0) + c_1(t - t_0)^2 \quad (14)$$

where  $c_0$  and  $c_1$  are adjustable parameters, and  $t_0$  is a partic-

<sup>3</sup> <http://www.mit.edu/~carterja/code/>

ular time near midtransit. In addition to the ramp correction, each light curve was described by an out-of-transit flux level  $F_0$  and midtransit time  $t_0$ . There were also 7 parameters common to all the light curves: the mean projected radius ratio  $R_{\perp}/R_*$  (where  $R_{\perp} = R_{\text{eq}}\sqrt{1-f_{\perp}}$ ), orbital inclination  $i$ , normalized orbital distance  $a/R_*$ , quadratic limb-darkening coefficients  $u_1$  and  $u_2$ , projected oblateness  $f_{\perp}$ , and projected obliquity  $\theta_{\perp}$ . The limb darkening coefficients parameterize the stellar brightness profile,  $I_*(r; u_1, u_2)$ , defined as

$$I_*(\mu; u_1, u_2) = I_*(1) [1 - u_1(1 - \mu) - u_2(1 - \mu)^2] \quad (15)$$

where  $\mu = \sqrt{1-r^2}$  and  $r$  is the sky-projected distance from the center of the star.

To derive the best-fitting parameter values we minimized the standard  $\chi^2$  statistic,

$$\chi^2 = \sum_{o=1}^7 \sum_{i=0}^{N_o} \left[ \frac{F_i^o(\text{obs}) - F_i^o(\text{calc})}{\sigma^o} \right]^2 \quad (16)$$

where  $o$  indexes the observation number,  $N_o$  is the number of data points in observation  $o$ ,  $F_i^o(\text{obs})$  is a measurement of the relative flux of HD 189733 during observation  $o$ ,  $F_i^o(\text{calc})$  is the calculated flux at that time according to the model, and  $\sigma^o$  is the uncertainty in flux measurement during observation  $o$ . We took  $\sigma^o$  to be the white noise amplitude of each time series as specified in § 3. As described above, we found the correlated noise component to be negligible. We minimized  $\chi^2$  using the AMOEBA routine (Press et al. 2007). The ramp-corrected light curves and the best-fitting model light curves are shown in Figure 2.

Then, after fixing the midtransit times, ramp correction parameters, and out-of-transit flux levels at the best-fitting values, we determined the credible intervals for the other parameters using a Markov Chain Monte Carlo (MCMC) algorithm.<sup>4</sup> We found that the quadratic limb darkening parameter was very poorly constrained by the data, and therefore for subsequent work we fixed that parameter at the value obtained in the preliminary fit. The parameters that were allowed to vary in the chain were  $R_{\perp}/R_*$ ,  $i$ ,  $a/R_*$ ,  $u_1$ ,  $T_0$ ,  $f_{\perp}$ , and  $\theta_{\perp}$ . Here,  $T_0$  represents an overall timing offset of all 7 transits, which is needed because the oblateness parameter is correlated with an overall time shift.

In the MCMC, the jump-transition probability was proportional to  $\exp(-\chi^2/2)$  with  $\chi^2$  given in Eqn. (16). We used Gibbs sampling in the construction of a chain of  $5 \times 10^5$  links. We selected individual parameter jump sizes such that the fraction of jumps accepted by a Metropolis-Hasting condition was between 30% and 60% for each parameter. Uniform priors were used for all parameters. We verified that the resulting posterior distributions had converged sufficiently.

Table 2 gives the results. For most parameters we report the median value of the posterior probability distribution, along with error bars defined by the 15.85% and 84.15% levels of the cumulative distribution. For the projected oblateness, we report the 95%-confidence upper limit. The projected obliquity was unconstrained. Figure (3) shows some of the posterior probability distributions. Figure 4 shows the constraints in the  $f_{\perp}-\theta_{\perp}$  plane. Only the results for  $\theta_{\perp} \geq 0$  are shown, as the constraints were found to be symmetric about  $\theta_{\perp} = 0$ . For

<sup>4</sup> For background on the MCMC method, see Gregory (2005), and for examples of applications to transit light curves, see Holman et al. (2006), Winn et al. (2007a), or Burke et al. (2007).

comparison, we have indicated in the figure the oblatenesses of Saturn, Jupiter and Uranus.

As anticipated from the theoretical work of Seager & Hui (2002) and Barnes & Fortney (2003), the projected oblateness is most tightly constrained when the projected obliquity is near  $45^\circ$ . We determined the 68% and 95% confidence regions in the  $f_{\perp}-\theta_{\perp}$  plane with the following technique. First, we divided the projected obliquity range into bins of constant width. Next, for the chain links in each bin, we sorted the values of  $f_{\perp}$  and determined  $f'_{\perp}$  such that 68% (95%) of the values were less than  $f'_{\perp}$ . Fig. (4) shows the resulting confidence curves.

Our analysis rules out a projected oblateness that is equal to Saturn's oblateness with  $>95\%$  confidence, regardless of the projected obliquity. A projected oblateness equal to Jupiter's oblateness is also ruled out with  $>95\%$  confidence, except for obliquities within about  $7^\circ$  of either  $0^\circ$  or  $90^\circ$ . For a projected obliquity near  $45^\circ$ , we may also exclude a projected oblateness equal to the oblateness of Uranus, with 95% confidence. Our constraints are consistent with the theoretical expectation that HD 189733b is rotating in synchrony with its orbit ( $f_{\perp} \approx f \approx 3 \times 10^{-3}$  and  $\theta_{\perp} \approx 0^\circ$ ).

The nondetection of oblateness suggests that the planet cannot be rotating too quickly, but the results cannot be translated directly into a lower bound on  $P_{\text{rot}}$  because of the sky projection. Even a very rapidly rotating (and very oblate) planet is consistent with the data as long as the planet's rotation axis is pointing at the observer ( $\theta = 90^\circ$  and  $\phi = 0$ ), leading to a circular projected figure. If we assume  $\theta \approx 0$  then we may set an upper bound on  $P_{\text{rot}}$ . We further assume that  $J_2$  is given by the Darwin-Radau relation (Eqn. 8), with  $\mathbb{C} = 0.225$ . Under these assumptions  $P_{\text{rot}} > 0.39$  d (9.4 hr) with 95% confidence. Larger values of  $\mathbb{C}$  would correspond to longer rotational periods. The median value of the posterior distribution is  $P_{\text{rot}}$  is 0.65 days, but we do not attribute any significance to that result, as the shape of the posterior distribution (including the median) is strongly affected by our assumption of a uniform prior in  $f_{\perp}$ . The lower bound on  $P_{\text{rot}}$  is less sensitive to the prior.

Conversely, if we assume HD 189733b to be synchronously rotating with zero obliquity and  $P_{\text{rot}} = 2.218573$  days, then we may place an upper bound on the rotationally-induced  $J_2$ , using Eqn. (6). The resulting posterior probability distribution for  $J_2$  is shown in Figure 5. We find that  $J_2$  must be smaller than 0.068 with 95% confidence. To place this in perspective, we note that if HD 189733b were a uniform-density sphere then under the same assumption of spin-synchrony and zero obliquity one would expect  $J_2 = 0.0018$ .<sup>5</sup> More centrally condensed planets would lead to smaller values of  $J_2$ . Hence, the empirical upper bound on  $J_2$  is not constraining on physically plausible models of the planet's interior.

#### 4.2. Uniform precession

As discussed in § 2.3, if HD 189733b is significantly oblate and oblique, then the spin axis will precess with a much shorter period than the precession periods of Saturn or Jupiter. The previous analysis assumed a fixed orientation for the planetary spin axis, and therefore the results must be understood as valid only for cases in which the precession period is much longer than 1 yr. The actual precession period depends on the internal constitution of the planet, specifically its mo-

<sup>5</sup> This was derived from Eqn. (3) of Ragozzine & Wolf (2009), using a Love number  $k_2 = 1.5$  for a uniform-density sphere.

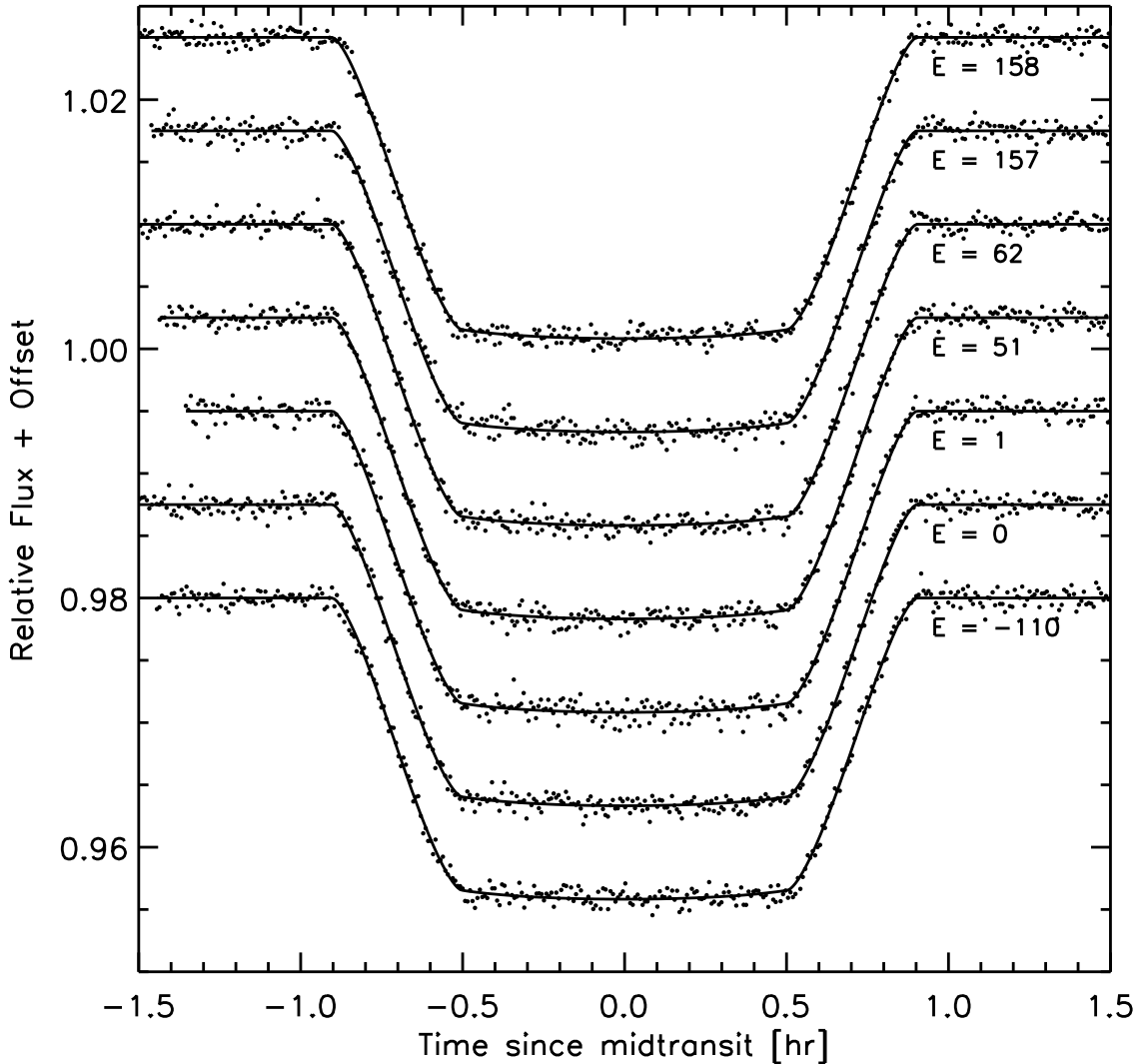


FIG. 2.— The relative  $8\ \mu\text{m}$  brightness of HD 189733 during 7 different transits of its giant planet, as measured with *Spitzer*/IRAC. The time series were corrected for the detector “ramp,” and offset in flux for display purposes. The solid curve is the best-fitting model. See § 4.1 for details.

ment of inertia and  $J_2$ . In the next part of our analysis we relaxed the assumption of a fixed orientation for the planetary spin axis, and allowed the axis to precess uniformly about the orbital axis.

We assumed that the *true* oblateness  $f$  and *true* obliquity  $\theta$  are constant in time, and allowed the azimuthal angle  $\phi$  to be a linear function of time,

$$\phi(t) = \frac{2\pi t}{P_{\text{prec}}} + \phi_0, \quad (17)$$

for some precession period  $P_{\text{prec}}$  and initial phase angle  $\phi_0$ . The time evolution of  $f_{\perp}$  and  $\theta_{\perp}$  are then given by Eqns. (9–10). A consequence of this time evolution is that the transit depth,  $\delta(t)$ , is variable. Apart from small corrections due to limb darkening, the transit depth is equal to the ratio of areas of the projected disks of the planet and star:

$$\delta(t) \approx \left(\frac{R_{\text{eq}}}{R_{\star}}\right)^2 [1 - f_{\perp}(t)]. \quad (18)$$

For large oblateness and obliquity, the transit depth variations can be easier to detect than the slight distortions in the ingress and egress portions of a single light curve. For a Saturn-like oblateness ( $f \approx 0.1$ ) at  $45^\circ$  obliquity, the transit depth variations are nearly 5% (see Fig. 6). For the 7 *Spitzer* time series, the transit depths were found to agree with one another to within 0.5%. This suggests that if HD 189733b were as oblate as Saturn and were also significantly oblique, then the spin-precession period must be much longer than 1.6 yr. For a quantitative and physically self-consistent analysis, we computed a second MCMC, using the parameters  $f$ ,  $\theta$ ,  $P_{\text{prec}}$  and  $\phi_0$  to describe the shape of the planet,<sup>6</sup> rather than the sky projected parameters  $f_{\perp}$  and  $\theta_{\perp}$ .

In principle, we could have used Eqn. (12) to enforce a relationship between  $P_{\text{prec}}$  and  $f$ , but that would have required some assumptions about the interior density structure of the planet. We preferred to allow  $P_{\text{prec}}$  to be a free parameter

<sup>6</sup> It proved advantageous to use  $R_{\text{eq}}\sqrt{1-f}$  as a fitting parameter, rather than  $R_{\text{eq}}$ , to reduce the correlation with  $f$ .

TABLE 2  
MODEL RESULTS: STATIC SHAPE PARAMETERS

Parameter	Median	Uncertainty
<i>Transit parameters:</i>		
$R_{\perp}/R_{\star}$	0.154679	$\pm 0.000067$
Orbital Inclination, $i$ [degrees]	85.749	$\pm 0.026$
$a/R_{\star}$	8.924	$\pm 0.022$
Projected oblateness $f_{\perp}$	0	$< 0.056$ (95% conf.)
Projected obliquity $\theta_{\perp}$	unconstrained	
<i>Limb darkening parameters:</i>		
Limb darkening parameter $u_1$	0.076	$\pm 0.011$
Limb darkening parameter $u_2$	0.034 (fixed)	–
Midtransit time shift $T_0$ [s]	0.0	$\pm 1.3$
<i>Derived parameters<sup>d</sup>:</i>		
Rotational Period [days] <sup>b,c</sup>	–	$> 0.39$ (95% conf.)
$J_2^d$	–	$< 6.8 \times 10^{-2}$ (95% conf.)

NOTE. — (a) Assuming zero obliquity. (b) Calculated using Eqn. (7) with  $R_{\star} = 0.756 R_{\odot}$ ,  $M_p = 1.144 M_{\text{Jup}}$  (Torres et al. 2008). (c) Assuming the validity of the Darwin-Radau approximation (Eqn. 8) with  $C = 0.225$ . (d) Calculated using Eqn. (6) assuming  $P_{\text{rot}} = P_{\text{orb}} = 2.218573$  days.

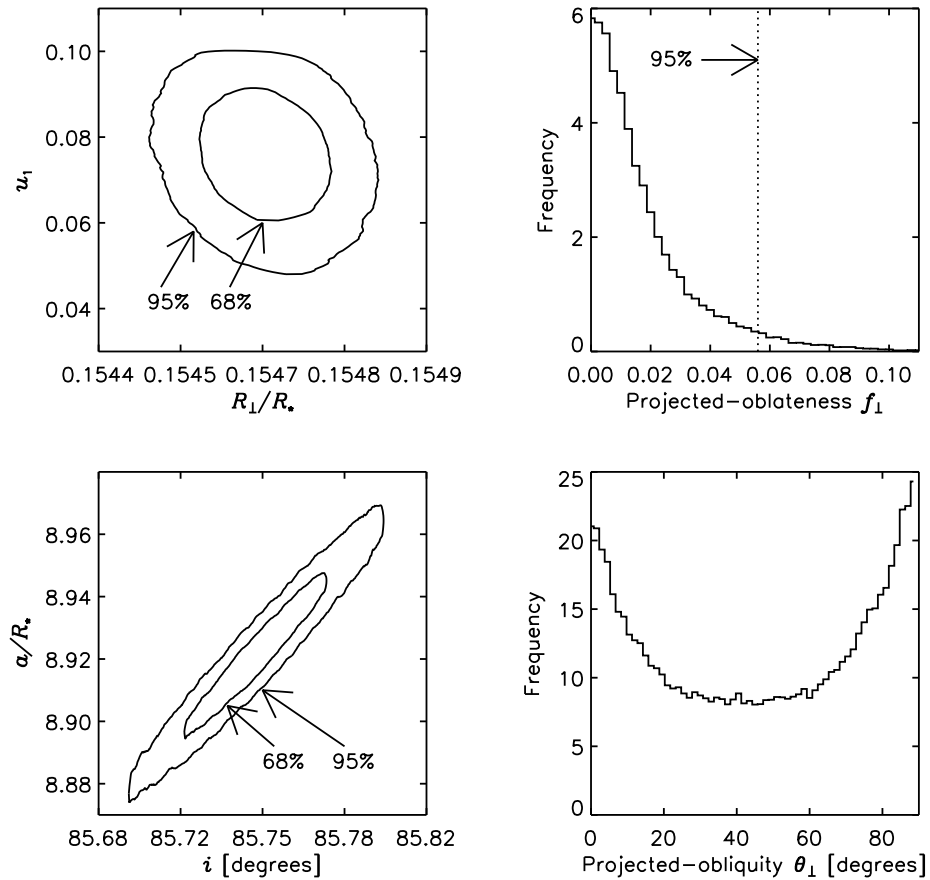


FIG. 3.— Joint confidence regions and posterior distributions for transit parameters and the projected shape parameters of HD 189733b, based on *Spitzer* observations of 7 transits. The shape parameters were assumed to be time-independent.

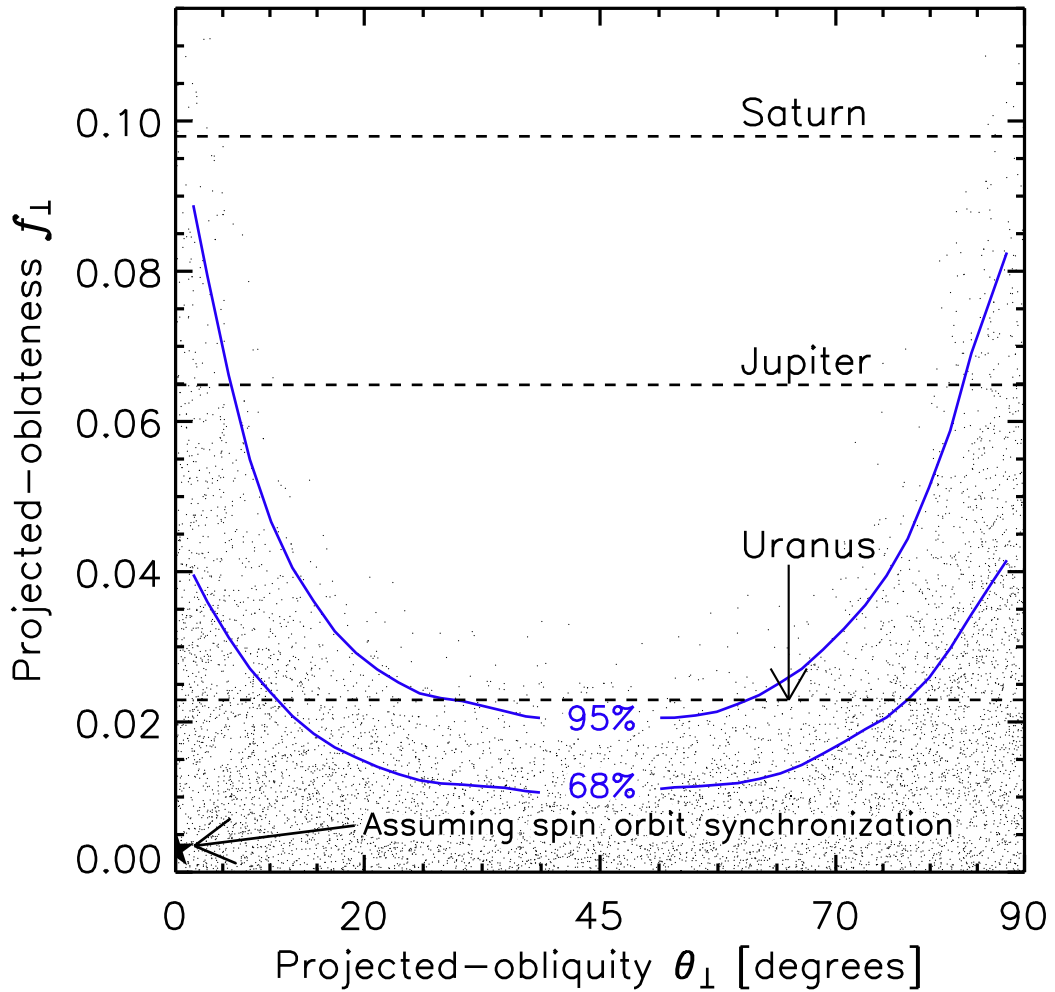


FIG. 4.— Posterior probability distribution for the projected oblateness and obliquity of HD 189733b, based on *Spitzer* observations of 7 transits. The shape parameters were assumed to be time-independent. The solid blue curves bound the regions containing 68% or 95% of the probability in the  $(f_{\perp}-\theta_{\perp})$  plane, marginalized over all other parameters. The black points are 10,000 representative values from the Markov chain, to illustrate the probability density. The star shows the expected shape parameters if HD 189733b is spin-orbit synchronized. The dashed lines indicate the oblateness of Jupiter, Saturn, and Uranus, for comparison.



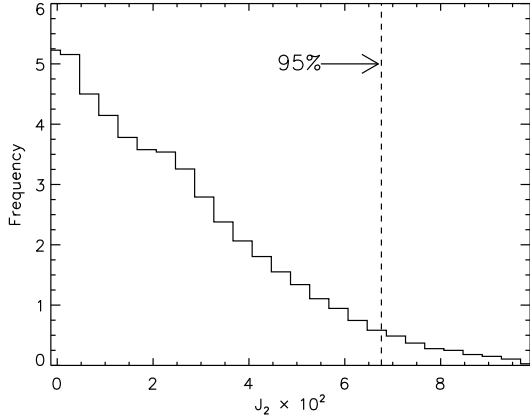


FIG. 5.— Posterior probability distribution for the quadrupole moment ( $J_2$ ) of HD 189733b. See § 4 for a discussion of the underlying assumptions in this calculation.

to avoid making such assumptions. The structure of close-in planets may differ from that of Jupiter and Saturn, due to a different history of formation and evolution, as well as the tidal influence of the parent star. We restricted our attention to  $P_{\text{prec}} < 10$  yr, because for longer precession periods the orientation of the spin axis would appear fixed over the 1.6 yr span of the *Spitzer* observations, and therefore our analysis would revert to that of the previous section.

We created two Markov chains, each with  $10^6$  links, and merged them after removing the first  $10^5$  links of each chain. The results are depicted in Fig. 6 as confidence regions in the  $f$ - $\theta$  plane. This figure is analogous to Fig. (4), although in this case we are constraining the true oblateness and obliquity as opposed to the projected quantities. Solutions with high oblateness and obliquity are ruled out by the observed absence of transit depth variations. Indeed, for  $P_{\text{prec}} < 10$  yr we can rule out a wider swathe of obliquity-oblateness parameter space than we did under the assumption of a nonprecessing planet.

For reference, Fig. 6 also shows contours indicating the amplitude of the expected transit depth variations, as well as contours indicating the spin precession period calculated from Eqn. (12), assuming  $C = 0.225$ . The precession period is smaller than 10 yr over more than 90% of the  $f$ - $\theta$  plane.

## 5. DISCUSSION

We have made the first attempt to measure the shape of a transiting exoplanet. Using *Spitzer* observations of 7 transits of HD 189733b, we have placed upper limits on the planet’s oblateness. The observed absence of lightcurve anomalies constrains the sky-projected oblateness and obliquity at each epoch. The collection of light curves spanning 1.6 yr constrains the true oblateness and obliquity, because spin precession would have produced transit depth variations in contradiction of the data. In both analyses an oblateness as large as that of Saturn could be ruled out with  $>95\%$  confidence.

<sup>7</sup> <http://kepler.nasa.gov/>; see also Borucki et al. (2009).

The resulting upper limits on the oblateness are physically meaningful, in the sense that they represent a physically possible degree of oblateness comparable to that of giant planets in the Solar system. However, for HD 189733b one would naturally expect a slower rotation rate and a smaller oblateness than those of Saturn or Jupiter, because tidal effects are expected to have slowed down the planetary rotation until it was synchronized with the orbital motion. Assuming that the planet is indeed spin-orbit synchronized with zero obliquity, we were able to place an upper bound on the quadrupole moment of the planet’s density distribution:  $J_2 < 6.8 \times 10^{-2}$  with 95% confidence. However this is a weak upper bound, in the sense that the theoretically expected value is at least an order of magnitude smaller.

The planet HD 189733b was chosen for this analysis because of the favorable stellar brightness and transit depth, as well as the large collection of high-quality data that are currently available for this system. However, this system suffers from the drawback that the theoretically expected oblateness is smaller than detection thresholds. The transiting planets HD 17156b (Barbieri et al. 2007) and HD 80606b (Moutou et al. 2009, Fossey et al. 2009, Garcia-Melendo & McCullough 2009) are attractive targets because they have much longer periods and higher orbital eccentricities than HD 189733b; although tidal evolution is expected to be important in both of those cases, it may have resulted in “pseudosynchronization” (Hut 1981) or some other state besides spin-orbit synchronization.

Furthermore, the *Kepler* mission<sup>7</sup> and other surveys for transiting planets should soon find planets with longer orbital periods and larger orbital distances, for which there is no reason to expect spin-orbit synchronization. There should be a “sweet spot” in orbital distance, far enough that the planet might be expected to rotate as rapidly as Jupiter or Saturn, yet close enough for the stellar gravitational field to cause relatively rapid spin precession that would be manifested as transit depth variations. A more general analysis of precession-induced transit depth variations seems warranted.

We are very grateful to Heather Knutson, Eric Agol, and their collaborators, for organizing the *Spitzer* observations. We are indebted to Dan Fabrycky for pointing out that spin precession can play an important role in the analysis. We thank Darin Ragozzine and the referee, Jason Barnes, for providing timely and detailed comments on the manuscript. We also benefited from discussions with Sara Seager and Saul Rappaport.

## APPENDIX

### A NUMERICAL ROUTINE FOR FAST, EFFICIENT CALCULATION OF TRANSIT LIGHT CURVES FOR OBLATE EXOPLANETS

In this appendix we describe a method for fast and stable calculations of light curves of ellipsoidal exoplanets, for which the sky projection is an ellipse. The development of this algorithm was crucial for our analysis, to make the MCMC method

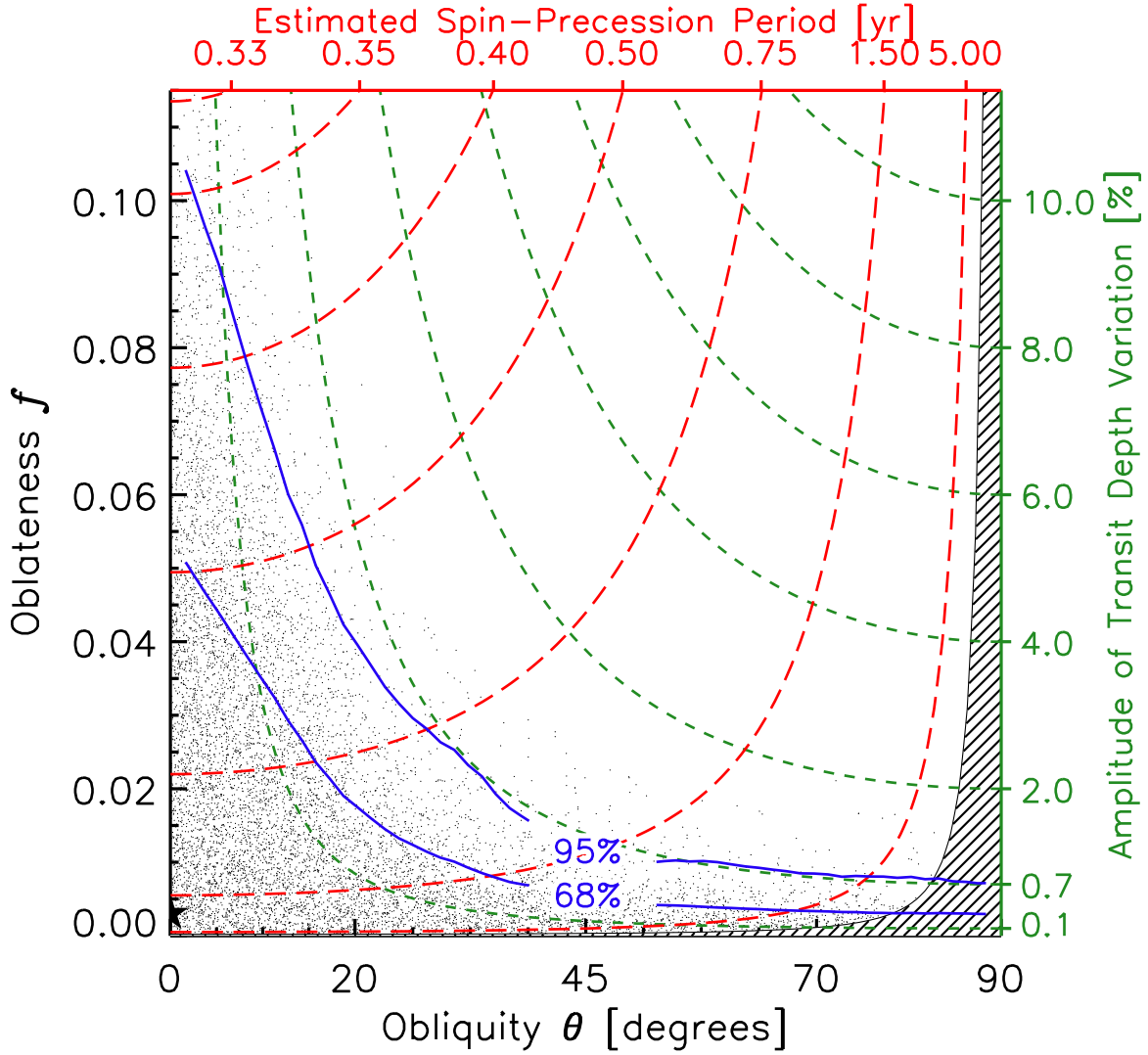


FIG. 6.— Constraints on the true oblateness and obliquity of HD 189733b, based on *Spitzer* observations of 7 transits. The solid blue curves bound the regions containing 68% or 95% of the MCMC samples in the oblateness-obliquity ( $f$ - $\theta$ ) plane. The black points are a random subsample of the full Markov chain, shown to illustrate the posterior probability density. The short-dashed green contours indicate the amplitude of transit depth variations. The long-dashed red contours show the expected spin-precession period, according to the formalism of § 2.3. The hatched region was not included in our analysis because the estimated precession period is  $>10$  yr.

computationally tractable. Proper convergence of these posterior distributions required many millions of executions of the light curve calculation. Seager & Hui (2002) and Barnes & Fortney (2003) both calculated light curves of oblate planets, but for those authors the computation time was probably of secondary importance.

Figure 7 illustrates the basic geometry of the calculation. An elliptical shadow with major and minor axes  $a$  and  $b$  obscures a portion of the circular stellar disk. The projected-oblateness  $f_{\perp}$  is defined as  $(a-b)/a$ . Distances are expressed in units of the stellar radius,  $R_{\star}$ . The semimajor axis of the ellipse is inclined by an angle  $\alpha$  from the line connecting the centers of the ellipse and circle. The angle  $\alpha$  is generally not the same as  $\theta_{\perp}$ , but the angles are equal for a central transit. The centers of the star and planet are separated by a distance  $x$ . We assume the stellar disk has a brightness profile  $I_{\star}(r, \theta)$  including, for example, a radial limb-darkening profile. The fractional flux deficit,  $F(x; a, b, \alpha, I_{\star})$ , due to the obscuring ellipse is

$$F(x; a, b, \alpha, I_{\star}) = \frac{1}{F_0} \int_{\mathcal{E} \cap \mathcal{C}} I_{\star}(r, \theta) r dr d\theta \quad (\text{A1})$$

where  $F_0$  is the total unobscured flux and the integral is performed over the region bounded by the intersection of the ellipse and circle, denoted as  $\mathcal{E} \cap \mathcal{C}$ . We consider a radial brightness profile given by a quadratic limb-darkening law,

$$\begin{aligned} I_{\star}(r, \theta) &= I_{\star}(r; u_1, u_2) \\ &= I_{\star}(1) \left[ 1 - u_1 \left( 1 - \sqrt{1-r^2} \right) - u_2 \left( 1 - \sqrt{1-r^2} \right)^2 \right] \end{aligned} \quad (\text{A2})$$

where  $u_1$  and  $u_2$  are the limb darkening parameters. With this law,  $F_0/I_{\star}(1) = \pi(1 - 1/3u_1 - 1/6u_2)$ . We denote the quadratic-profile

fractional flux deficit by the form  $F(x; a, b, \alpha, u_1, u_2)$ . For  $a = b = R_p/R_*$ ,  $F(x; a, u_1, u_2) \equiv F(x; a, a, \alpha, u_1, u_2)$  has a closed-form analytic solution in terms of elliptic integrals (Mandel & Agol 2002). The problem is more complicated for arbitrary  $a$ ,  $b$ ,  $\alpha$ ,  $u_1$  and  $u_2$  since the vertices of the intersection region  $\mathcal{E} \cap \mathcal{C}$  cannot always be determined analytically, and the integral cannot be done in closed form.

There are standard routines for computing the intersections of two ellipses that would allow us to define the intersection region  $\mathcal{E} \cap \mathcal{C}$  (see, e.g., Hill 1994). We found, however, that these algorithms are not numerically stable over the entire region of parameter space of interest. We chose to sacrifice runtime to ensure stability by finding the intersections of a polygonal representation of the obscuring ellipse and the disk, as follows. First, we analytically find the coordinates in the  $x$ - $y$  plane of points on the boundary of the ellipse at  $N$  uniformly selected angles (from 0 to  $2\pi$ ). Next, these points in the plane are connected by line segments. Finally, the routine accumulates approximate intersections of the ellipse and circle by determining the intersections of each line segment and the circle. We use  $N \approx 200$  to ensure adequate precision.

With the points of intersection determined, we move on to the calculation of the integral in Eqn. (A1). Before discussing the general problem, we first consider the case of uniform brightness ( $u_1 = u_2 = 0$ ) and solve for  $F(x; a, b, \alpha, 0, 0)$ . Here, solving the integral in Eqn. (A1) is equivalent to finding the area of the region  $\mathcal{E} \cap \mathcal{C}$ . This area may be calculated analytically by using the formula for the area of an elliptical chord  $A(\theta_1, \theta_2, a, b)$ :

$$A(\theta_1, \theta_2, a, b) = ab[(\theta_1 - \theta_2) - \sin(\theta_1 - \theta_2)]/2 \quad (\text{A3})$$

where the angles  $\theta_{1,2}$  are measured relative to the semi-major axis. To solve for  $F(x; a, b, \alpha, 0, 0)$  we add the area of the elliptical chord (defined by the lines connecting the intersection points<sup>8</sup> and the curve bounding the ellipse that is internal to the stellar disk) to the area of the circular chord (defined by the complement of this elliptical chord and  $\mathcal{E} \cap \mathcal{C}$ ).

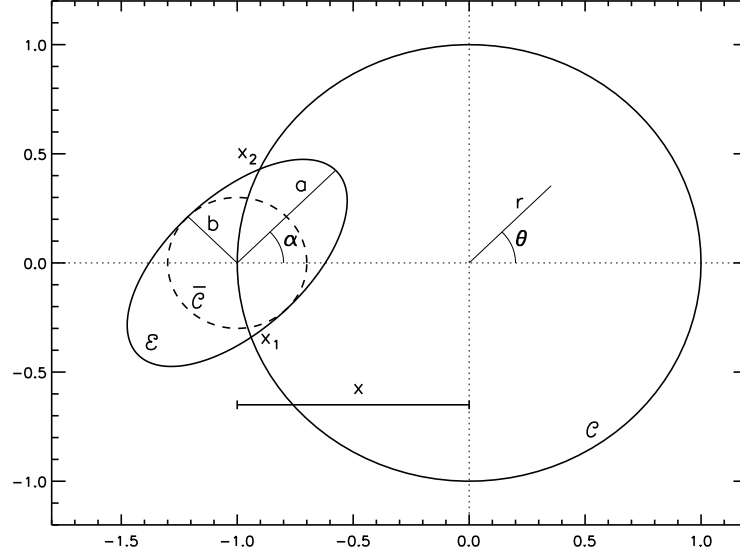


FIG. 7.— Geometry of the transit of an ellipsoidal planet across a circular stellar disk. The deficit in flux due to the obscuring ellipse with semi-major axis  $a$ , semi-minor axis  $b$  and orientation  $\alpha$  a distance  $x$  from the center of the star may be found by integrating the brightness profile of the star over the intersection region of the ellipse  $\mathcal{E}$  and circle  $\mathcal{C}$ . The ellipse and circle intersect at points  $x_{1,2}$ . A closed-form solution for the flux deficit exists for the inscribed circle  $\bar{\mathcal{C}}$  of radius  $b$ . Only the intersection region less this circle,  $\mathcal{E}/\bar{\mathcal{C}} \cap \mathcal{C}$  needs to be integrated numerically.

Next, consider the integral given by Eqn. (A1) for nonzero  $u_1$  and  $u_2$ . Numerical integration must be performed. We could perform two-dimensional numerical integration over  $\mathcal{E} \cap \mathcal{C}$  [as was done by Seager & Hui (2002)] or numerically integrate in the radial direction, calculating the intersections of circle and ellipse at each integration step [as was done by Barnes & Fortney (2003)]. For our application we chose the former, although because of the difficulty in specifying the integration region, we found standard deterministic integration techniques to be too slow.

Instead, we chose to use Monte Carlo integration [see, e.g., Press et al. (2007)]. With Monte Carlo integration, the integral  $\int_{\mathcal{A}} f(x, y) dx dy$  over the region  $\mathcal{A}$  is calculated by sampling the function  $f(x, y)$  at  $N$  uniformly distributed random points in a region  $\mathcal{R}$  that covers  $\mathcal{A}$ . When a sample  $(x, y)$  is drawn from  $\mathcal{R}$  that is not in  $\mathcal{A}$ , we set  $f(x, y) = 0$ . According to the fundamental theorem of Monte Carlo integration,

$$\int_{\mathcal{A}} f(x, y) dx dy \approx \text{Area}[\mathcal{R}] \left[ \langle f \rangle \pm \sqrt{\frac{\text{Var}(f)}{N}} \right]. \quad (\text{A4})$$

<sup>8</sup> In general, a circle and an ellipse may intersect at up to four distinct locations; for an exoplanet with small oblateness and  $R_p \approx R_{\text{Jupiter}}$  orbiting a star with  $R_* \approx R_{\odot}$ , only two intersections (at most) are expected.

The means are calculated over the  $N$  randomly sampled points (Press et al. 2007). In general, Monte Carlo integration is reserved for integrals of high dimensionality due to its slow convergence ( $1/\sqrt{N}$ ) compared to more traditional methods when calculating two-dimensional integrals. For our purposes, Monte Carlo integration reduces the difficulty associated with bounding the intersection region  $\mathcal{E} \cap \mathcal{C}$ . An improvement in convergence ( $\sim 1/N$ ) is obtained by sampling  $\mathcal{R}$  “quasi-randomly” as opposed to randomly, using a low-discrepancy random sequence called the Sobol’ sequence (Sobol’ & Shukhman 1995, Press et al. 2007). The Sobol’ sequence is a sequence of uniformly distributed values on the unit interval,  $s_i$  for  $i \geq 0$ , such that a given sequence member at index  $I$  is *maximally* distant from all previous samples  $i < I$ .

To simplify the computational effort required for the integral of Eqn. (A1) when using the quadratic limb-darkened profile [Eqn. (A2)], we rewrite the integral as

$$\begin{aligned}
F(x; a, b, \alpha, u_1, u_2) &\times \pi \left(1 - \frac{u_1}{3} - \frac{u_2}{6}\right) \\
&= \int_{\mathcal{E} \cap \mathcal{C}} 1 - u_1 (1 - \sqrt{1 - r^2}) - u_2 (1 - \sqrt{1 - r^2})^2 r dr d\theta \\
&= (1 - u_1 - u_2) \left( \int_{\mathcal{E} \cap \mathcal{C}} r dr d\theta \right) \\
&\quad + \int_{\mathcal{E} \cap \mathcal{C}} \left[ (u_1 + 2u_2) \sqrt{1 - r^2} - u_2 (1 - r^2) \right] r dr d\theta \\
&= (1 - u_1 - u_2) \times F(x; a, b, \alpha, 0, 0) \\
&\quad + \int_{\mathcal{E} \cap \mathcal{C}} \hat{I}_*(r; u_1, u_2) r dr d\theta
\end{aligned} \tag{A5}$$

where  $F(x; a, b, \alpha, 0, 0)$  is the uniform-brightness solution (calculated as described above) and  $\hat{I}_*(r; u_1, u_2) = (u_1 + 2u_2) \sqrt{1 - r^2} - u_2 (1 - r^2)$  describes the nonuniform component of the brightening profile.  $\hat{I}_*(r = 1; u_1, u_2) = 0$  at the stellar limb. The remaining unknown integral is over a function that has low variance over any bounding region  $\mathcal{R}$  covering the limb, making the absolute error in the Monte Carlo integration smaller (for a fixed  $N$ ) as compared to integrating  $I_*$  in full.

Note that the only portion that requires numerical integration is the intersection region excluding the circle  $\bar{\mathcal{C}}$  of radius  $b$  inscribed in  $\mathcal{E}$  [see Fig. (7)]. We denote this smaller region by  $\mathcal{E}/\bar{\mathcal{C}} \cap \mathcal{C}$ . The integral over  $\bar{\mathcal{C}}$  is analytic, as per Mandel & Agol (2002), and is denoted  $F(x; b, u_1, u_2)$ . Thus Eqn. (A5) becomes

$$\begin{aligned}
F(x; a, b, \alpha, u_1, u_2) &\times \pi \left(1 - \frac{u_1}{3} - \frac{u_2}{6}\right) \\
&= (1 - u_1 - u_2) \times [F(x; a, b, \alpha, 0, 0) - F(x; b, 0, 0)] \\
&\quad + F(x; b, u_1, u_2) \\
&\quad + \int_{\mathcal{E} \cap \mathcal{C}/\bar{\mathcal{C}}} \hat{I}_*(r; u_1, u_2) r dr d\theta.
\end{aligned} \tag{A6}$$

The only nontrivial component is the final term, which we denote  $\mathcal{I}$  and for which we use quasi-Monte Carlo integration. For slightly oblate exoplanets or weakly limb-darkened brightness profiles, the contribution of this integral in the total flux deficit is small compared to the remaining terms in Eqn. (A6). The absolute contribution of this term to the flux deficit is bounded by

$$\begin{aligned}
\frac{1}{\pi} \left(1 - \frac{u_1}{3} - \frac{u_2}{6}\right)^{-1} \mathcal{I} &\leq \frac{u_1 + 2u_2}{1 - 1/3u_1 - 1/6u_2} \times (ab - b^2) \\
&= ab f_{\perp} \frac{u_1 + 2u_2}{1 - 1/3u_1 - 1/6u_2}.
\end{aligned} \tag{A7}$$

For comparison, the size of the flux deficit in the absence of limb-darkening is  $ab$ .

To calculate  $\mathcal{I}$  via quasi-Monte Carlo integration, we select a covering region,  $\mathcal{R} \supset \mathcal{E}/\bar{\mathcal{C}} \cap \mathcal{C}$ , that efficiently bounds the integration region and that can be easily sampled with the Monte Carlo technique ( $\mathcal{E}/\bar{\mathcal{C}} \cap \mathcal{C}$  cannot). Here, easily sampled means that we may take a two dimensional Sobol’ sequence, uniform in  $[0, 1] \times [0, 1]$ , and analytically transform it such that the transformed sequence uniformly samples our chosen covering region. A uniform sampling on the unit square may be mapped to a uniform sampling over a region bounded by an elliptical annular sector (see Appendix B for details). An elliptical annular sector is the region bounded between two concentric ellipses (i.e., two ellipses with coincident centers and equal axis ratios and position angles) with semi-major axes  $a_1 < a_2$  and by the rays (emanating from the common center) at angles  $\theta_1, \theta_2$  relative to the semi-major axis. The formulae for the specific values of  $\theta_1, \theta_2, a_1$  and  $a_2$  as functions of the parameters  $x, a, b$ , and  $\alpha$  for use in the integration routine are chosen from one of the following cases [with reference to Fig. (8)]:

- (I) *One or fewer intersections between circle and ellipse.*
  - (a)  $x > 1$ ; The obscuring ellipse is external to the circle,  $\mathcal{I} = 0$ .
  - (b)  $x < 1$ ; The obscuring ellipse is properly contained in the circle;  $\theta_1 = 0, \theta_2 = 2\pi, a_1 = b, a_2 = a$ .
- (II) *Two points of intersection between circle and ellipse.*

The circle and ellipse intersect at  $x$ -coordinates  $x_{1,2}$  at angles  $\theta'_{1,2}$  from the  $x$ -axis.

(a)  $x > 1$ ; For each intersection  $x$ -coordinate  $x' = x_i$ , angle  $\theta' = \theta'_i$  and final solution angle  $\theta = \theta_i$ :

(1)  $|x| > |1/x'|$ ; The line connecting the point of intersection and the ellipse center [at  $(x,0)$ ] intersects the circle exactly once:  $\theta = \theta' - \alpha$ .

(2)  $|x| < |1/x'|$ ; The line connecting the point of intersection and the ellipse center [at  $(x,0)$ ] intersects the circle twice: use  $\theta = \hat{\theta} - \alpha$  where the angle  $\hat{\theta} = \tan^{-1} 1/\sqrt{1-x^2}$  defines the line segment that connects the ellipse center and the point of tangency on the circle.

If  $a'$  is the semi-major axis of the concentric ellipse “kissing” the circle<sup>9</sup> then  $a_1 = \max(b, a')$ ,  $a_2 = a$ .

(b)  $x < 1$ ; Use the angle  $\theta_b$  defined by the intersection points of the inscribed circle with radius  $b$  ( $\bar{\mathcal{C}}$ ) and the stellar disk ( $\mathcal{C}$ ):  $\theta_{1,2} = \pm\theta_b - \alpha$ ,  $a_1 = b$ ,  $a_2 = a$ .

By choosing the elliptical annular sector as defined above as the bounding region for the the desired integration region ( $\mathcal{E}/\bar{\mathcal{C}} \cap \mathcal{C}$ ), we ensure that the integration region covers approximately 50% of the bounding region regardless of the values of  $x$ ,  $a$ ,  $b$ , and  $\alpha$ .

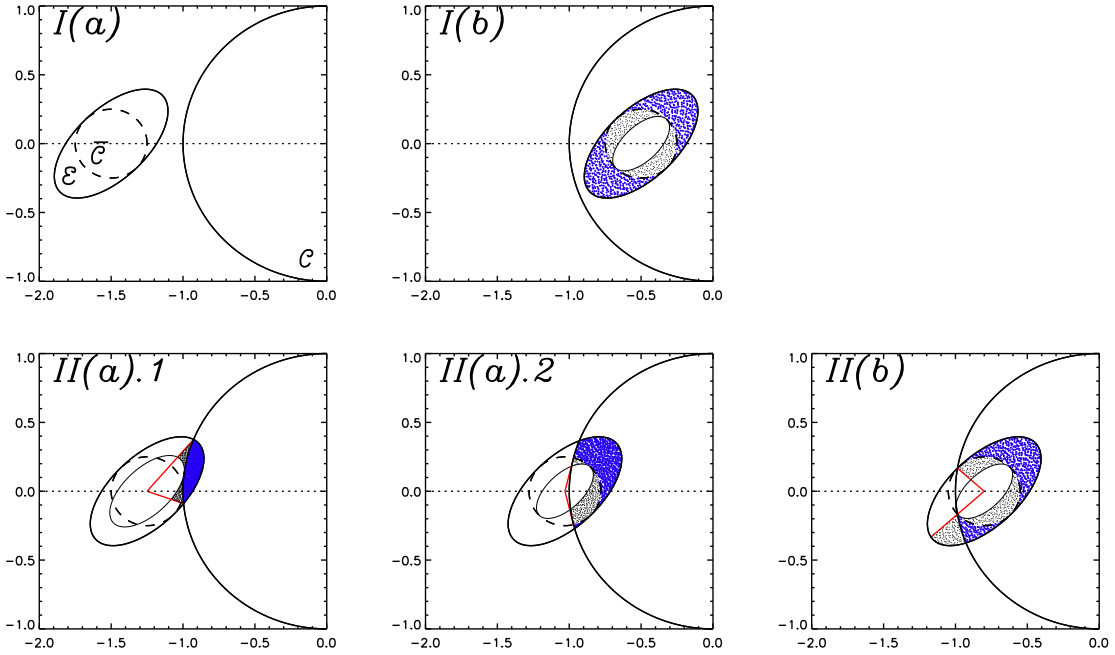


FIG. 8.— Quasi-Monte Carlo integration of the nontrivial component of the total flux deficit for the stellar transit of an oblate planet. These figures show the transit phases and quasi-Monte Carlo integration regions described in Appendix A, which are needed to evaluate the nontrivial integral  $\mathcal{I}$  [see Eqn. (A6)]. The labels in the upper left hand corners of each figure correspond to those in the text. In each figure, the inner ellipse with semi-major axis  $a_1$  gives the inner boundary of the elliptical annular sector. The red rays emanating from the ellipse indicate the angular extent of the sector (with angles  $\theta_{1,2}$  relative to the semi-major axis). The blue or black points are 1000 uniformly distributed Sobol’ points in the elliptical annular sector. The blue points are those which fall in the integration region  $\mathcal{E}/\bar{\mathcal{C}} \cap \mathcal{C}$ .

To give some idea of the computation time, we consider the case  $x = 1$ ,  $a = 0.155$ ,  $b = 0.148$ ,  $u_1 = 0.2$ ,  $u_2 = 0.3$ , and  $\alpha = 0.5$ , corresponding to an oblate ( $f_{\perp} = 0.05$ ) version of HD 189733b. Using a C++ implementation of our algorithm on a 2.6 GHz Intel Core 2 Duo MacBook Pro, it takes 0.5 ms to compute  $F$  with a precision of 1 ppm. For comparison, it takes 0.004 ms to execute the same computation for a spherical planet, using the Fortran implementation of the code by Mandel & Agol (2002).

#### UNIFORM SAMPLING OF AN ELLIPTICAL ANNULAR SECTOR

##### *Elliptical annular sector*

A point  $(x, y)$  is inside the elliptical annular sector centered at  $(0, 0)$  with semi-major axis in the  $x$ -direction, axis ratio  $\epsilon$ , inner radius  $a_1$ , outer radius  $a_2$ , and sector angles  $\theta_{1,2}$  if the all of following conditions are satisfied:

$$(1) \quad \frac{x^2}{a_1^2} + \frac{y^2}{(\epsilon a_1)^2} > 1 \quad (\text{B1})$$

<sup>9</sup> “Kissing” ellipses intersect at exactly one point. The “kissing” ellipse’s semi-major axis  $a'$  for this application is found with a linear search.

$$(2) \frac{x^2}{a_2^2} + \frac{y^2}{(\epsilon a_2)^2} < 1 \quad (\text{B2})$$

$$(3) \text{ The line connecting } (0, 0) \text{ to } (x, y) \text{ is at an angle } \theta \text{ relative to the } x\text{-axis such that } \theta_2 > \theta > \theta_1 \quad (\text{B3})$$

An elliptical annular sector is illustrated in Fig. (9).

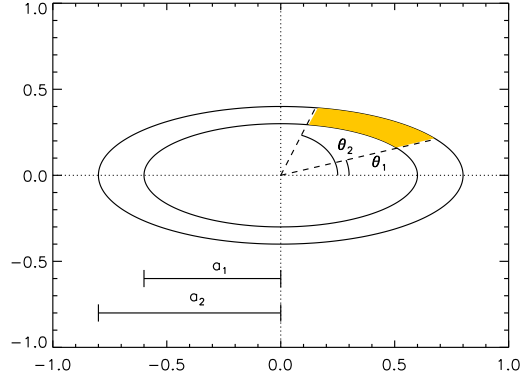


FIG. 9.— An elliptical annular sector.

#### Uniform sampling

Let  $(u, v)$  be a uniform sample of the unit square  $[0, 1] \times [0, 1]$ . Then  $(u', v')$  is a uniform sample of the elliptical annular sector where

$$u' = a_2 r \cos(\theta) \quad (\text{B4})$$

$$v' = \frac{a_2 r}{\epsilon} \sin(\theta) \quad (\text{B5})$$

and

$$r = \sqrt{(1-u) a_1^2 + u} \quad (\text{B6})$$

$$\theta = (1-v) \tan^{-1}(\epsilon \tan \theta_1) + v \tan^{-1}(\epsilon \tan \theta_2). \quad (\text{B7})$$

#### REFERENCES

- Agol, E., Cowan, N. B., Bushong, J., Knutson, H., Charbonneau, D., Deming, D., & Steffen, J. H. 2009, IAU Symposium, 253, 209
- Barbieri, M., et al. 2007, A&A, 476, L13
- Barnes, J. W. 2009, ApJ, 705, 683
- Barnes, J. W., & Fortney, J. J. 2003, ApJ, 588, 545
- Beaulieu, J. P., Carey, S., Ribas, I., & Tinetti, G. 2008, ApJ, 677, 1343
- Borucki, W. J., and 24 colleagues 2009. Kepler's Optical Phase Curve of the Exoplanet HAT-P-7b. Science 325, 709.
- Bouchy, F., et al. 2005, A&A, 444, L15
- Burke, C. J., et al. 2007, ApJ, 671, 2115
- Carter, J. A., & Winn, J. N. 2009, ApJ, 704, 51
- Désert, J.-M., Lecavelier des Etangs, A., Hébrard, G., Sing, D. K., Ehrenreich, D., Ferlet, R., & Vidal-Madjar, A. 2009, ApJ, 699, 478
- Eddington, A. S. 1926, The Internal Constitution of the Stars, Cambridge: Cambridge University Press, 1926.
- Fabrycky, D. C., Johnson, E. T., & Goodman, J. 2007, ApJ, 665, 754
- Fazio, G. G., et al. 2004, ApJS, 154, 10
- Fossey, S. J., Waldmann, I. P., Kipping, D. M. 2009, MNRAS, 396, L16
- Garcia-Melendo, E., McCullough, P. R. 2009, ApJ, 698, 558
- Gillon, M., et al. 2007, A&A, 471, L51
- Goldreich, P., & Soter, S. 1966, Icarus, 5, 375
- Gregory, P. C. 2005, Bayesian Logical Data Analysis for the Physical Sciences: A Comparative Approach with *Mathematica* Support (Cambridge Univ. Press, UK).
- Guillot, T., Burrows, A., Hubbard, W. B., Lunine, J. I., & Saumon, D. 1996, ApJ, 459, L35
- Hellier, C., et al. 2009, Nature, 460, 1098
- Hill, Kenneth J., Graphics Gems V, ed A.W. Paeth, Orlando, Academic Press, Inc., 1994, p. 72-77
- Høg, E., et al. 2000, A&A, 355, L27
- Holman, M. J., et al. 2006, ApJ, 652, 1715
- Hubbard, W. B. 1984, Planetary Interiors, New York, Van Nostrand Reinhold Co.
- Hubbard, W. B., & Marley, M. S. 1989, Icarus, 78, 102
- Hut, P. 1981, A&A, 99, 126
- Knutson, H. A., et al. 2007a, Nature, 447, 183
- Knutson, H. A., Charbonneau, D., Noyes, R. W., Brown, T. M., & Gilliland, R. L. 2007b, ApJ, 655, 564
- Levrard, B., Correia, A. C. M., Chabrier, G., Baraffe, I., Selsis, F., & Laskar, J. 2007, A&A, 462, L5
- Lindal, G. F., et al. 1981, J. Geophys. Res., 86, 8721
- Lindal, G. F., Sweetnam, D. N., & Eshleman, V. R. 1985, AJ, 90, 1136
- Mandel, K., & Agol, E. 2002, ApJ, 580, L171
- Miller-Ricci, E., et al. 2008, ApJ, 682, 593
- Moutou, C., et al. 2009, A&A, 498, L5
- Murray, C. D., & Dermott, S. F. 2000, Solar System Dynamics, by C.D. Murray and S.F. Dermott. Cambridge, UK: Cambridge University Press, 2000.,
- Nutzman, P., Charbonneau, D., Winn, J. N., Knutson, H. A., Fortney, J. J., Holman, M. J., & Agol, E. 2009, ApJ, 692, 229
- Peale, S. J. 1999, ARA&A, 37, 533
- Pont, F., et al. 2007, A&A, 476, 1347

- Press, William H., Teukolsky, Saul A., Vetterling, William T., & Flannery, Brian P. 2007, *Numerical Recipes: The Art of Scientific Computing*, 3rd ed. (New York: Cambridge University Press)
- Ragozzine, D., & Wolf, A. S. 2009, *ApJ*, 698, 1778.
- Seager, S., & Hui, L. 2002, *ApJ*, 574, 1004
- Sobol', I. M., & Shukhman, B. V. 1995, *International Journal of Modern Physics C*, 6, 263
- Torres, G., Winn, J. N., & Holman, M. J. 2008, *ApJ*, 677, 1324
- Ward, W. R. 1975, *Science*, 189, 377
- Ward, W. R., & Hamilton, D. P. 2004, *AJ*, 128, 2501
- Winn, J. N., Holman, M. J., & Roussanova, A. 2007, *ApJ*, 657, 1098
- Winn, J. N., et al. 2007, *AJ*, 133, 1828
- Winn, J. N., et al. 2009, *ApJ*, 703, 2091
- Winn, J. N., & Holman, M. J. 2005, *ApJ*, 628, L159